[Supplementary material]

Early settlement construction in Southeast Asia: lime mortar floor sequences at Loc Giang, southern Vietnam

Elle Grono[1,3,*][ORCID: 0000-0002-3607-6686], Philip J. Piper[1], Dang Ngoc Kinh[2], Peter Bellwood[1][ORCID: 0000-0001-6033-9629], Tim Denham[1][ORCID: 0000-0002-8164-2990] & David E. Friesem[3,4,5][ORCID: 0000-0002-5541-6156]

[1] School of Archaeology and Anthropology, Australian National University, Canberra, Australia

[2] Center for Archaeological Studies, Southern Institute for Social Sciences, Ho Chi Minh City, Vietnam

[3] Department of Maritime Civilizations, School of Archaeology and Maritime Cultures, University of Haifa, Israel

[4] Recanati Institute of Maritime Studies, University of Haifa, Israel

[5] Haifa Center for Mediterranean History, University of Haifa, Israel

[*] Author for correspondence ✉ Egrono@campus.haifa.ac.il

OSM 1: methodological protocols

Micromorphology

Floor surface samples were prepared into thin sections following standard fabrication procedures (Courty *et al*. 1989) and analysed under low magnification up to 40× using a low-powered Olympus SZ-40 stereomicroscope and high magnification from 20× to 400× using an Olympus CX31 optical polarising microscope. Thin sections were described using international descriptive protocols (Stoops 2003) with reference to published archaeological micromorphology guides (Courty *et al*. 1989; Macphail & Goldberg 2017; Nicosia & Stoops 2017) including micromorphological identification of lime floors (Karkanas 2007; Stoops *et al*. 2017). Thin sections were digitised using an Epson perfection V700 flatbed scanner and photomicrographs were imaged with an Olympus CS30 3MP camera and processed using Olympus Stream V1.9.1 software.

Automated Quantitative Evaluation of Minerals using Energy Dispersive Spectroscopy (QEM-EDS)

QEM-EDS analyses were conducted on two polished and carbon-coated billets using an FEI

Quanta QEMSCAN® system. Data were collected in field image scan mode using 15kV accelerating voltage and a 10nA probe current. A total of 2000 X-ray counts were collected at each analysis point using a 15µm spacing interval. FEI iMeasure software was used for data acquisition, FEI iDiscover software for raw data processing, and Nanomin software (Version 1.3.2) for mineral classifications and for generating elemental and mineral distribution maps. SEM-EDS point analyses, conducted using a Hitachi 4300 SE/N Schottky Field Emission Scanning Electron Microscope, collected quantitative elemental data to assist in QEM-EDS mineral classifications.

Fourier-Transform Infrared (FTIR) spectroscopy

FTIR was conducted on 26 samples using small amounts (10–20mg) of extracted sediments prepared following the potassium bromide (KBr) method (Weiner 2010). A Thermo Nicolet iS5 spectrometer was used to collect spectra between 4000 and 400cm^{-1} at 4cm^{-1} resolution. Spectra were interpreted with reference to Weiner (2010) and the Kimmel Center for Archaeological Science Infrared Standards Library, Weizmann Institute of Science.

X-ray Diffraction (XRD)

XRD was performed on two floor samples using a SIEMENS D501 Bragg-Brentano diffractometer with a graphite monochromator and scintillation detector and Cu K-α radiation. Samples were scanned at 4° to 84° 2-theta at a step width of 0.02° and a scan speed of 1° per minute. Standard pre-treatment and analytical protocols for clay identification was carried out on one sample (Moore & Reynolds 1989). The results were interpreted using the Bruker AXS software package Diffracplus Eva 10.0.

Biogenic silica concentrations

Biogenic silica bodies were extracted from 20–50mg of sediment from five floor samples and one modern control sample following the laboratory procedure established by Katz *et al*. (2010). Phytoliths and diatoms were counted in 16 fields using an Olympus CX31 light microscope at 200× magnification and concentrations were calculated using the equation formulated by Katz *et al*. (2010: 1558).

OSM2: micromorphological descriptions

Table S1. Micromorphological descriptions of lime-rich archaeological contexts from Loc Giang. Microstratigraphic units (MSU) refer to individual microlayers within thin sections. The coarse-to-fine (C/F) limit is set at 10µm. Percentages refer to the amount of a given component as a proportion of the total area of the MSU.

Microstratigraphic Unit (MSU)	Summary of micromorphological attributes	Deposit type	Interpretation
14_6.2, 14_6.4, 14_7.2, 14_13.2, F-95, F-97.2, F-99.2, F-99.4, F-110.2, F-113.2, F-113.3, F-117.2	**Thickness:** 8–55 mm. **Boundaries:** sharp and horizontal, locally biologically reworked. **Microstructure:** Massive, apedal. Coarse components are randomly-oriented and distributed (Figure S1a–S1b). *Voids:* 5–20%: Planar and sub-horizontal fissures (2–10%, some MSUs show dominant horizontal orientation (e.g. Figure S1h), other MSUs show random to oblique orientation) (Figure S1g); moldic voids (pseudomorphic and shrinkage voids after vegetal matter) (2–5%); vughs and vesicles (1–5%) (Figure S1c); biological channels and modified planar voids (0–10%). **Coarse/fine:** *C/F ratio:* 40:60 to 60:40. *C/F related distribution:* porphyric. **Fine material:** *Colour and composition:* speckled to cloudy, pale grey to orange-brown (PPL), cream and orange (OIL) microcrystalline calcium carbonate. *B-fabric:* crystallitic, varying from well-reacted to mottled isotropic (Figures S1a-S1d). **Coarse components:** *Mineral:* quartz (1–5%, 30 –350µm); sandstone clasts (1–5%, 800–2000µm) (Figure S2h). *Biomineral:* charred plant fragments (2–5%, <6000µm) (Figure S2a); silicified plant remains (2–5%, elongated fibres, cell structure and articulated phytoliths) (Figure S2d); vitrified phytolith slags (2–5%) (Figure S2f); rice husks (2%, observed as silicified, carbonised, or as rice husk pseudomorphic voids) (Figures S2b, S2e); bone (1–2%, leached, <3mm, rare burnt bones) (Figure S2j); Shell (1–2%, <4200µm) (Figure S2k); calcitic ashes (1%, in anatomical position within charred plant structures) (Figure S2b–S2c). *Organic:* coprolites (2–5%, <13mm) (Figure S2l); degrading and humified organic residues (2–5%, amorphous orange-yellow to reddish brown (PPL), fibrous structures). *Anthropogenic:* clay	*Lime mortar floor*	Constructed lime mortar floors, exhibiting a microcrystalline calcium carbonate matrix including mottled, isotropic areas from incomplete carbonation of lime, small aggregates of quicklime (calcium oxide), and isotropic reaction rims. The floors were tempered with a range of inclusions: dominant fired clay construction aggregates;

	construction aggregates (2–15%, densely packed fabric, plant temper or silt–size quartz inclusions, pinkish orange to deep red (PPL), variably rubified (orange–crimson (OIL)), some show shrinkage/reticulate alteration patterns from heat alteration and isotropic reaction rims, 150–8000µm) (Figure S2g); reaction rims on components and possible quicklime lumps (2–5%, <2800µm) (Figure S1d–S1e); pottery (1–2%, 350–7000µm) (Figure S2i). **Pedofeatures:** *Textural:* pale limpid (PPL) rims around clay aggregates (2%, grano-striated b-fabric (XPL), effect of firing or wetting/drying); translocated clay coatings on voids (1%). *Crystalline:* recrystallised calcite (micritic and sparitic calcitic coatings and infillings in voids and precipitation in the matrix, some MSUs (e.g. MSU F117.2) show increased porosity from calcitic dissolution). *Amorphous and cryptocrystalline:* localised phosphatic enrichment of the groundmass and inclusions (cryptocrystalline pinkish-orange (PPL), isotropic (XPL)); Fe-Mn oxide nodules, precipitation of the fine material, coatings on coarse components, and pseudomorphic replacement of organic residues. *Excrement:* discontinuous infillings of excremental microaggregates and crumbs in biological voids.		common plant materials; and, infrequent to rare fragments of bone, shell, pottery and coprolites. Thicknesses of the floors are *c*. 8–55mm. Some floors exhibit sub-horizontal fissures attributed to trampling.
F-117.1	**Thickness:** 5mm thick. **Boundaries:** sharp. Lower boundary meets MSU 117.2. **Microstructure:** Massive, composed of undulating microlaminations. *Voids:* <5%: planar cracks (2%, horizontally-oriented); vesicles (2%). **Coarse/fine:** *C/F ratio:* 5:95. *C/F related distribution:* porphyric. **Fine material:** *Colour and composition:* microcrystalline calcium carbonate, exhibiting different purities and colours ranging from translucent light grey through to cloudy and opaque dark brownish grey (PPL) (Figure S3c). Micromass locally exhibits zigzag reticulate patterning (Figure S3d). Opaque dark grey (PPL) isotropic (XPL) fine textures may be unreacted or partially reacted quicklime. *B-fabric:* crystallitic, varying from well-reacted to transitional and isotropic (Figure S3c–S3d). **Coarse components:** *Mineral:* quartz (5%, 30–200µm). **Pedofeatures:** *Crystalline:* recrystallised calcitic domains showing changes in size and purity of crystals (Figure S3c). *Amorphous and cryptocrystalline:* Fe-Mn oxide staining of the groundmass.	*Lime plaster coating*	Microlayer (<5mm thick) identified as a lime wash across the upper surface of a constructed lime mortar floor [F-117].

F-141	**Microstructure:** Massive, apedal. *Voids:* 5%: planar cracks (2%); vesicles (2%); vughs (1%). **Coarse/fine:** *C/F ratio:* 10:90. *C/F related distribution:* porphyric. **Fine material:** *Colour and composition:* microcrystalline calcium carbonate. *B-fabric:* crystallitic, well-reacted. **Coarse components:** *Mineral:* quartz (2%; 50–400µm); sandstone clasts (2%, 800–7400µm). *Biomineral:* siliceous plant remains and phytoliths (2–5%) (Figure S4e); bone fragments (2%, <2000µm) (Figure S4d); calcitic ash rhombs (1%) (Figure S4e). *Organic:* dark brown (PPL) amorphous organic elongated fibres (2%). **Pedofeatures:** *Crystalline:* recrystallised calcitic domains showing changes in size and purity of crystals. Secondary calcitic coatings on voids (2%). *Amorphous and cryptocrystalline:* Fe-Mn oxide diffuse staining, dendritic nodules, coatings and replacement of organic residues (5%).	*Residual lime waste*	White powdery chunk of lime, probably residual from lime production. Combusted and ashed plant remains and bone fragments appear as additives to the lime paste.

OSM3: micromorphology photomicrographs

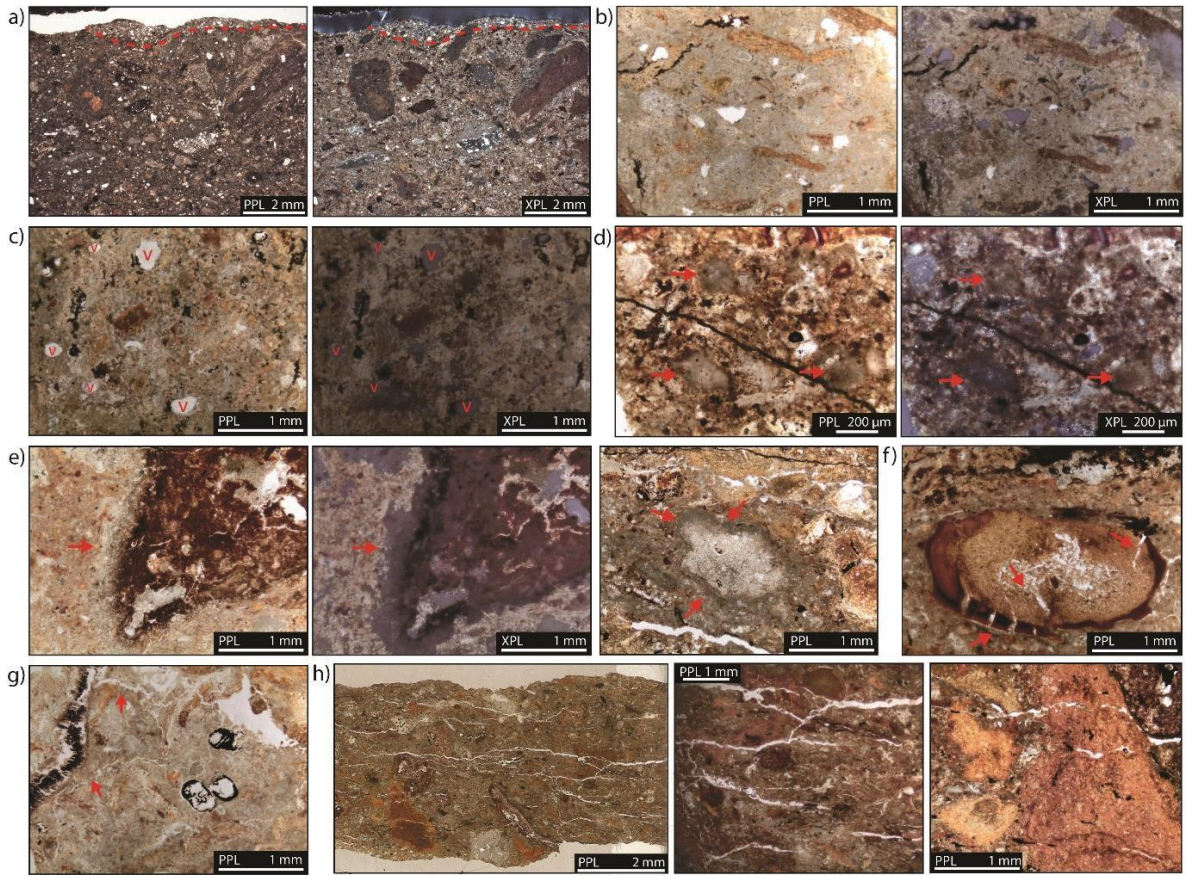

Figure S1. Binder properties and evidence of lime production in the lime mortar floors: a) floor surface showing a sharp upper surface and a dense, compacted microstructure with low porosity and evenly mixed coarse inclusions. Minimal accumulation of well-sorted detrital mineral grains (dashed red line) indicate the floors were kept clean through sweeping or use of mats; b) binder exhibits a well-reacted microcrystalline calcium carbonate (XPL) groundmass and evenly mixed coarse temper including fired clay and quartz mineral grains; c) and d) occasional local domains show mottled, hazy, semi-isotropic (XPL) transitional textures from incomplete reaction; c) shows vesicles (v) from trapped air in the lime paste and (d) depicts small possible quicklime (calcium oxide) aggregates from incomplete carbonation; e) isotropic (XPL) unreacted lime rims from reactions between coarse components and lime binder; f) darkened and cracked rims around a clay aggregate caused by heat alteration; g) fine planar fissures in the binder formed from drying and hardening of the lime; h) horizontal fissures through a lime mortar floor attributed to vertical pressure from trampling. The fissures move through and cleave apart coarse components, such as the clay construction aggregates depicted here, rather than skirting components (image by E. Grono).

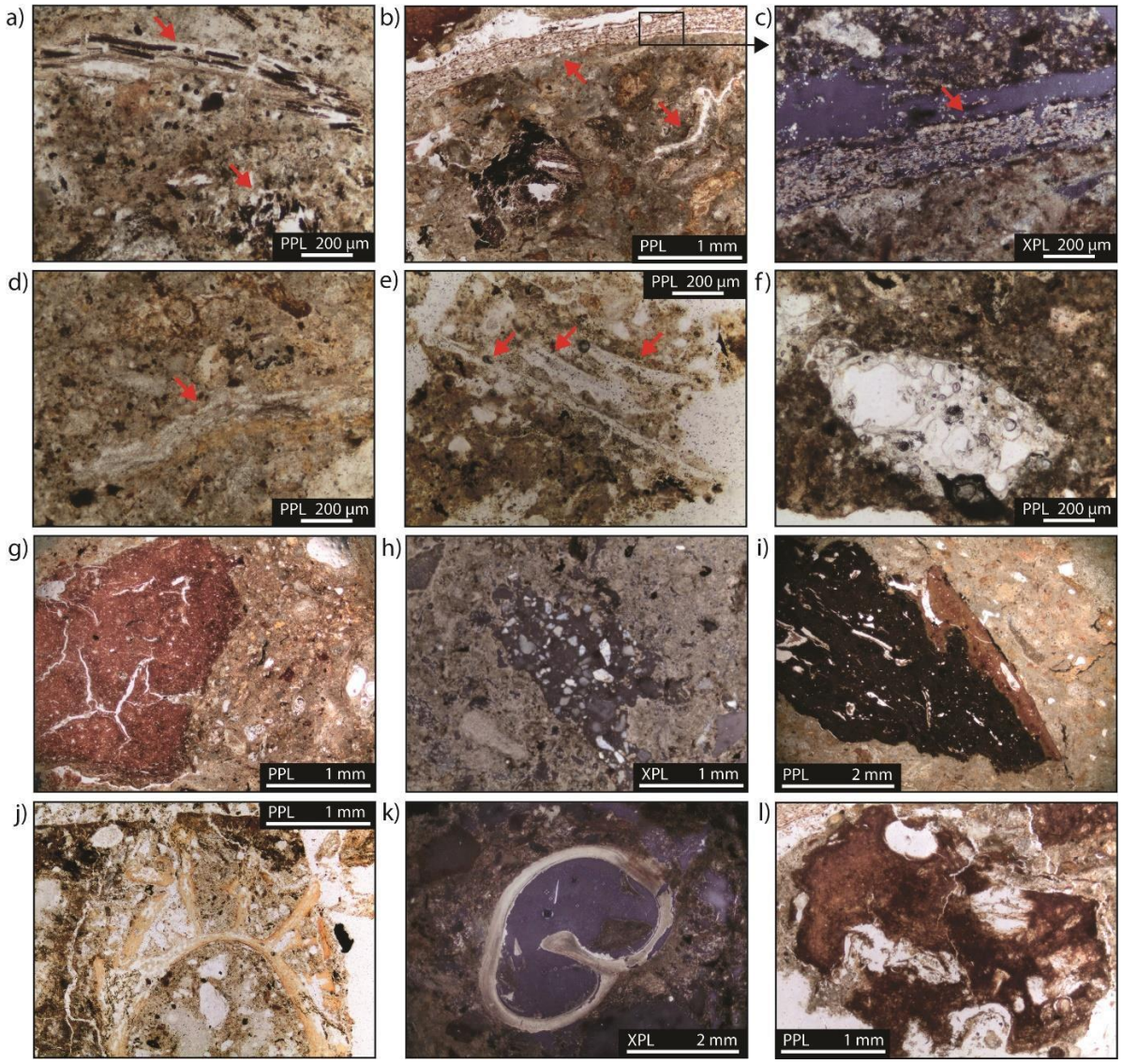

Figure S2. Additive materials in the lime mortar floors: a) and b) charred plant remains in shrinkage voids; b) (bottom arrow) siliceous rice husk; c) plant materials shown in (b) under magnification, showing calcitic plant ashes in anatomical position within charred plant structures; d) phytoliths, articulated; e) three silicified rice husks; f) melted phytolith slag showing a morphology of vesicular silica; g) clay aggregate rubified by exposure to heat and showing shrinkage cracks from firing; h) sandstone clast; i) fibre-tempered ceramic fragment; j) vertebrae bone fragment; k) shell fragment; l) coprolite fragment with indicative internal voids containing fibrous organic matter (image by E. Grono).

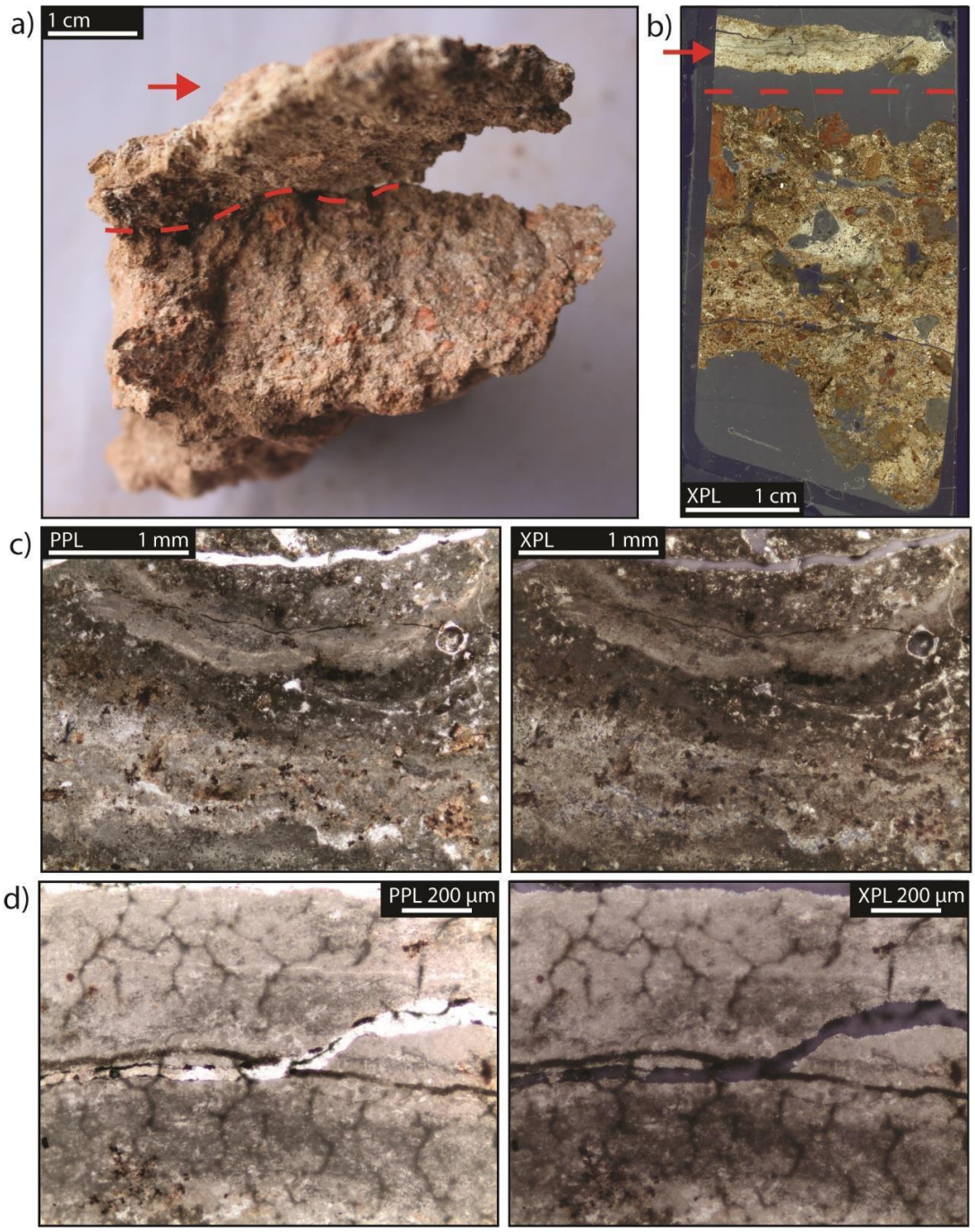

Figure S3. Lime plaster coating or wash: a) macro-lens photograph showing adherence of the coating (red arrow) to the upper surface of a constructed lime mortar floor [F-117] (red dashed line); b) XPL thin section scan showing a well-reacted fine calcitic groundmass of the lime plaster coating (red arrow); c) the lime coating comprises microlaminations of different colour and purity of microcrystalline calcium carbonate. Microlaminations formed as a result of the application of several washes or from several cycles of wetting and weathering during burial; d) zigzag to reticulate patterning in the reacted lime from carbonation, either during original hardening of the slaked lime, or possibly forming as a post-depositional feature following wetting (image by E. Grono).

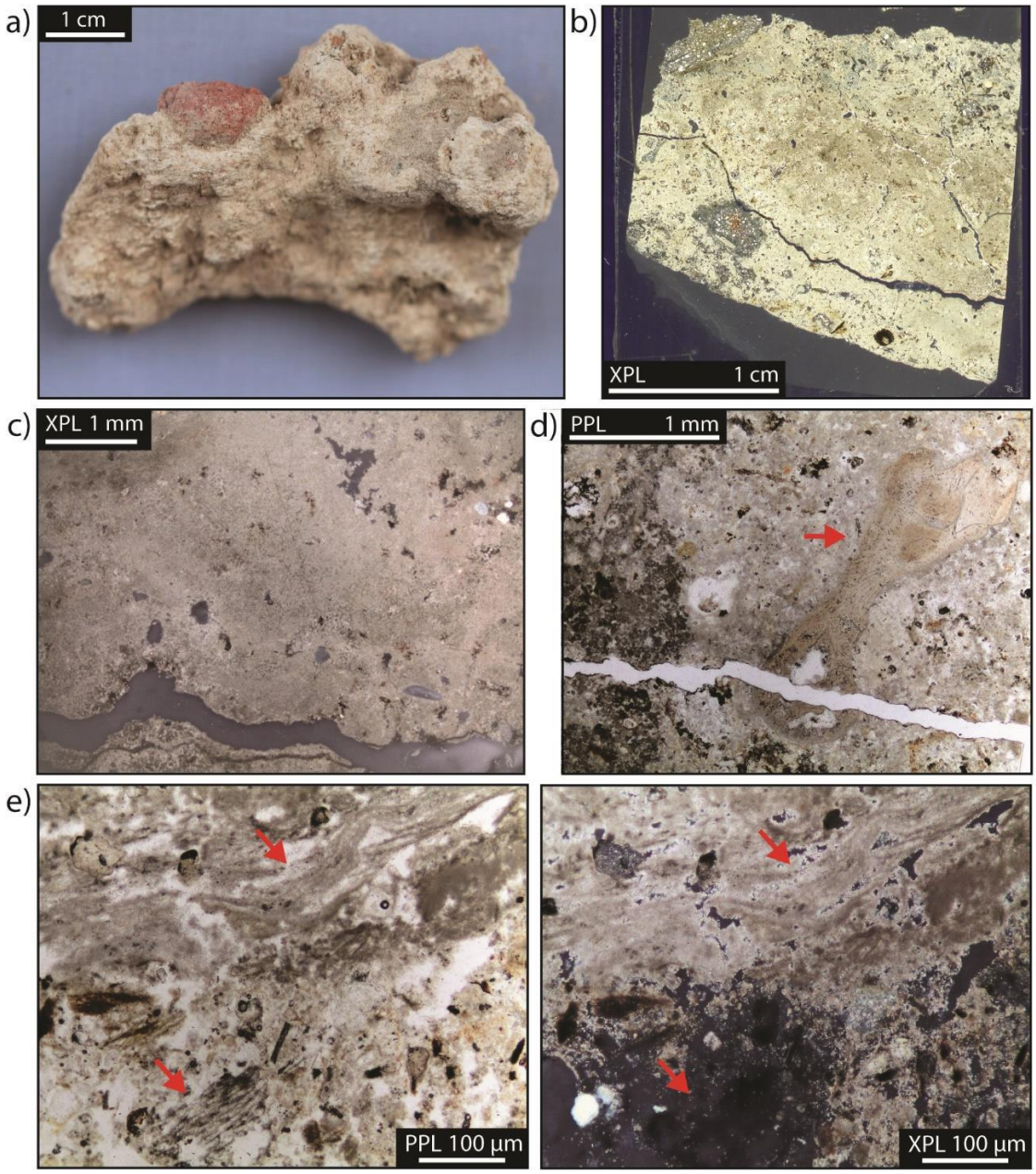

Figure S4. Lime chunk identified as residual waste from lime preparation: a) macro-lens photograph showing the powdery cream fine texture with visible aggregates of fired clay; b) XPL thin section scan, and (c) XPL photomicrograph showing a dense microcrystalline calcium carbonate groundmass with almost complete recarbonation of lime; d) a bone fragment embedded in the groundmass; e) plant materials including calcitic plant ashes in anatomical position (top arrow, possibly recrystallised in situ) and articulated phytoliths (bottom arrow, isotropic in XPL) (image by E. Grono).

OSM4: X-ray Diffraction (XRD) diffractograms

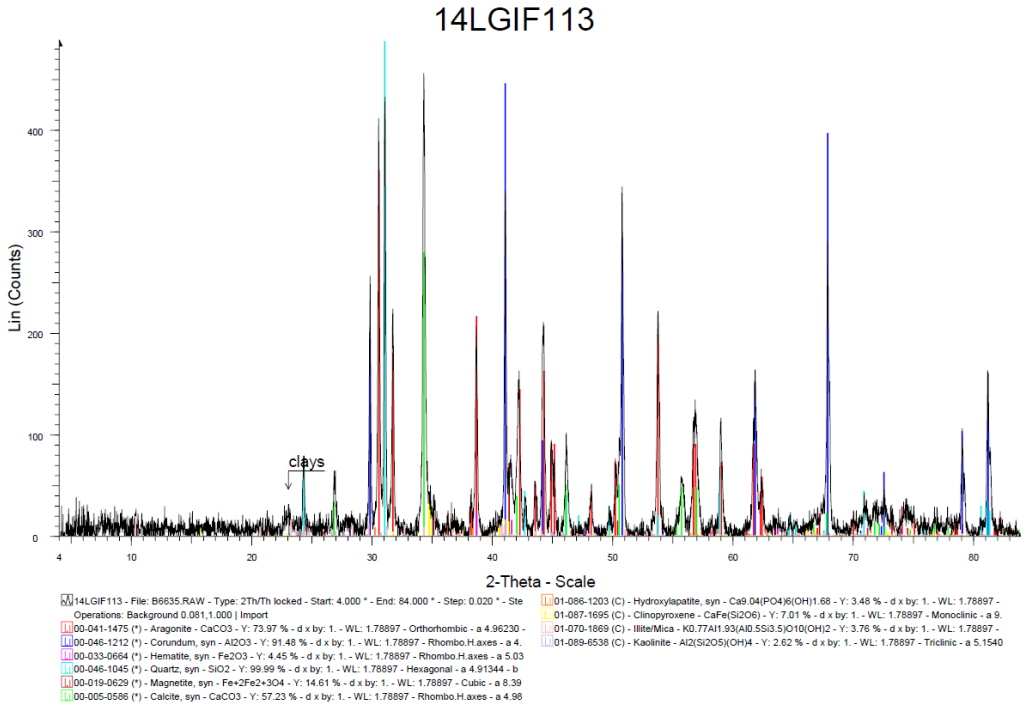

Figure S5. XRD diffractogram of F-113 (lime mortar floor) from the 2014 excavation at Loc Giang (image by U. Troitzsch and E. Grono).

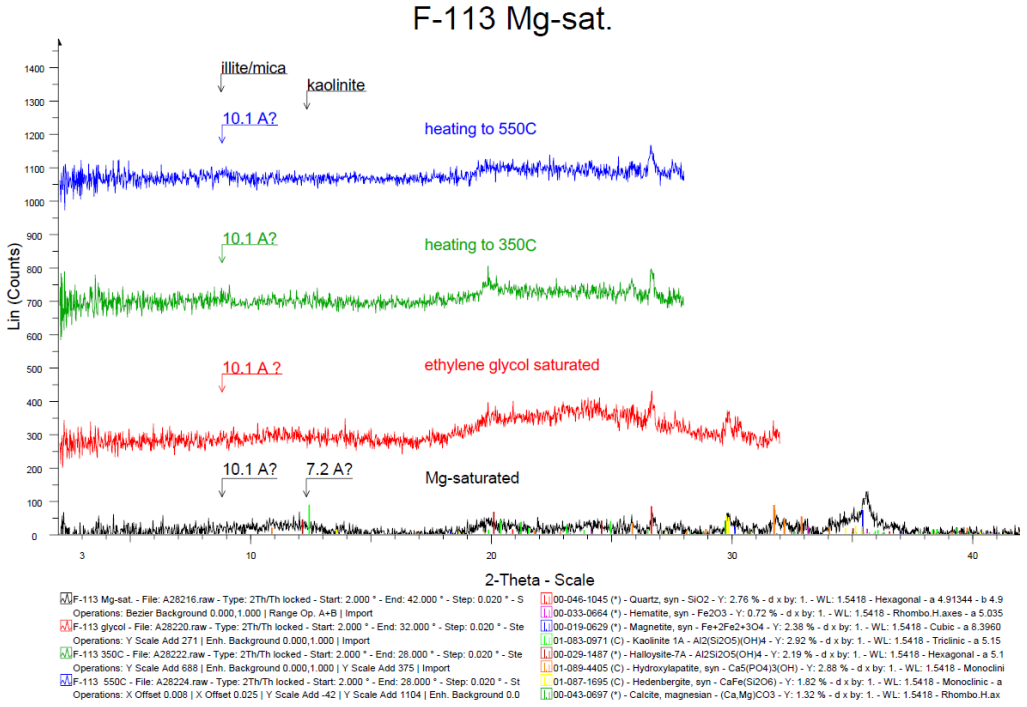

Figure S6. Clay mineral identification of F-113 (lime mortar floor) from Loc Giang by XRD, showing the behaviour of clays after a series of pre-treatment steps. The black diffractogram shows the normal XRD pattern without clay pre-treatment. The red diffractogram shows the XRD pattern after solvation of the sample with ethylene glycol. The green diffractogram

shows the XRD pattern after heating the sample at 350°C for two hours. The blue diffractogram shows the XRD pattern after heating the sample at 550°C for two hours (image by U. Troitzsch and E. Grono).

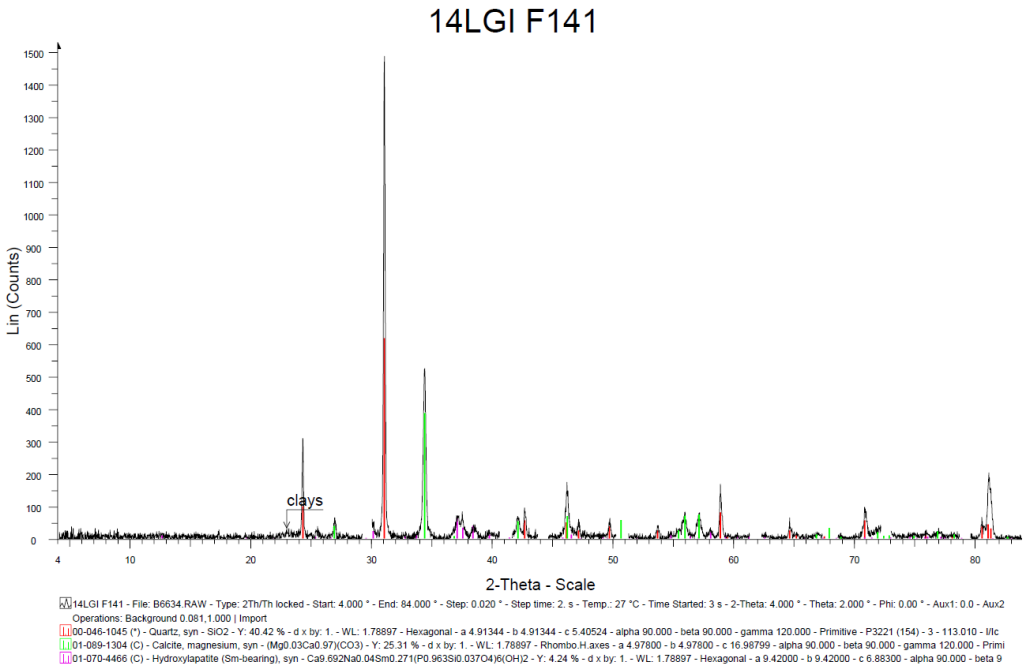

Figure S7. XRD diffractogram of F-141 (residual lime chunk) from the 2014 excavation at Loc Giang (image by U. Troitzsch and E. Grono).

OSM5: Fourier-Transform Infrared (FTIR) spectroscopy

Table S2. FTIR spectral identifications of lime-rich archaeological contexts from Loc Giang. Minerals are listed in order of abundance based on relative peak height. Each sample is allocated an alphabetical code in the rightmost column to denote a spectral compositional group and representative spectral image shown in Figure S8. Arg = aragonite; Cal = calcite; CHAP = carbonate hydroxyapatite; Dol = dolomite; Hem = hematite; Qtz = quartz. Clay alteration state: Cl(n.a.) = clay not altered (not heated); Cl(s.a.) = slightly altered clay (possibly altered (heated) clay; however, the mixture of altered and non-altered clay or other materials masks the signal of heat-induced clay alteration); Cl(a) = altered clay (heated). * = Traces in the sediments, indicated by small peaks only.

Context	Sample description	Deposit type	Sample type			Minerals	Spectral group (Figure S8)
			Intact feature deposit	Micromorphology block	Ceramic sherd		
6.2	Floor matrix	Lime mortar floor		✓		Cl(a.) > Arg > Cal	D
6.4	Floor matrix	Lime mortar floor		✓		Cl(a.) > Arg > Cal. Qtz* CHAP*	D
6.4	Floor inclusion: aggregate	Lime mortar floor		✓		Cl(s.a.)	B
7.2	Floor matrix	Lime mortar floor		✓		Cl(s.a.). Cal* Arg*	B
7.2	Floor inclusion: shell fragment	Lime mortar floor		✓		Cal	E
13.2	Floor inclusion: red aggregate	Lime mortar floor		✓		Cl(a.)=Qtz	F
F-95	Floor matrix	Lime mortar floor	✓			Dol > Cal > Arg > Cl(a.). CHAP*	H
F-95	Floor inclusion: white aggregate	Lime mortar floor	✓			Cl(a.) > Cal	D
F-97.2	Floor matrix	Lime mortar floor	✓			Cl(a.) > Cal. Qtz* CHAP*	D

F-97.2	Floor inclusion: brownish-black aggregate	Lime mortar floor	✓			Cl(n.a.) > Qtz. Hem	C
F-97.2	Floor inclusion: greenish-black aggregate	Lime mortar floor	✓			Cl(n.a.) > Qtz. Hem	C
F-97.2	Floor inclusion: orange aggregate	Lime mortar floor	✓			Cl(a.)	A
F-97.2	Floor inclusion: pink aggregate	Lime mortar floor	✓			Cl(a.). Cal*	A
F-97.2	Floor inclusion: pinkish aggregate	Lime mortar floor	✓			Cl(a.). Cal* CHAP*	A
F-99.2	Floor matrix	Lime mortar floor	✓			Cl(a.) > Arg > Cal. CHAP*	D
F-99.4	Floor matrix	Lime mortar floor	✓			Arg > Cal > Cl(a.). CHAP*	G
F-99.4	Floor: pink aggregate	Lime mortar floor	✓			Cl(a.) > Arg > Cal. CHAP*	D
F-110.2	Floor matrix	Lime mortar floor	✓			Arg > Cl(a.). CHAP*	G
F-110.2	Floor matrix: red aggregate	Lime mortar floor	✓			Cl(a.)	A
F-113.1	Compacted sediment on floor surface	Lime mortar floor	✓			Arg > Cal > Cl(a.). CHAP*	G
F-113.1	Rubified sediment on floor surface	Lime mortar floor	✓			Cl(a.) > Arg > Cal. Hem	D
F-113.1	Compacted whitish-grey sediment on floor surface	Lime mortar floor	✓			Cal > Arg > Cl(a.). CHAP*	G
F-117.1	White coating on floor surface	Lime plaster coating	✓			Cal > Cl(a.). CHAP*	G
F-117.2	Floor matrix	Lime mortar floor	✓			Arg > Cl(a.). CHAP*	G
F-117.2	Floor inclusion: pinkish orange aggregate	Lime mortar floor	✓			Cl(a.) > Qtz	F
F-141	Whitish grey cemented sediment	Residual lime waste	✓			Cal > CHAP > Cl(a.)	I
C.102	Sand tempered pottery	Pottery – fired clay			✓	Cl(a.). Hem	A
C.103	Rice tempered pottery	Pottery – fired clay			✓	Cl(a.) > Qtz	A
C.108	Rice tempered pottery	Pottery – fired clay			✓	Cl(a.)	A
C.110	Sand tempered pottery	Pottery – fired clay			✓	Cl(a.). Hem	A

C.112	Rice tempered pottery	Pottery – fired clay			✓	Cl(a.). Hem	A

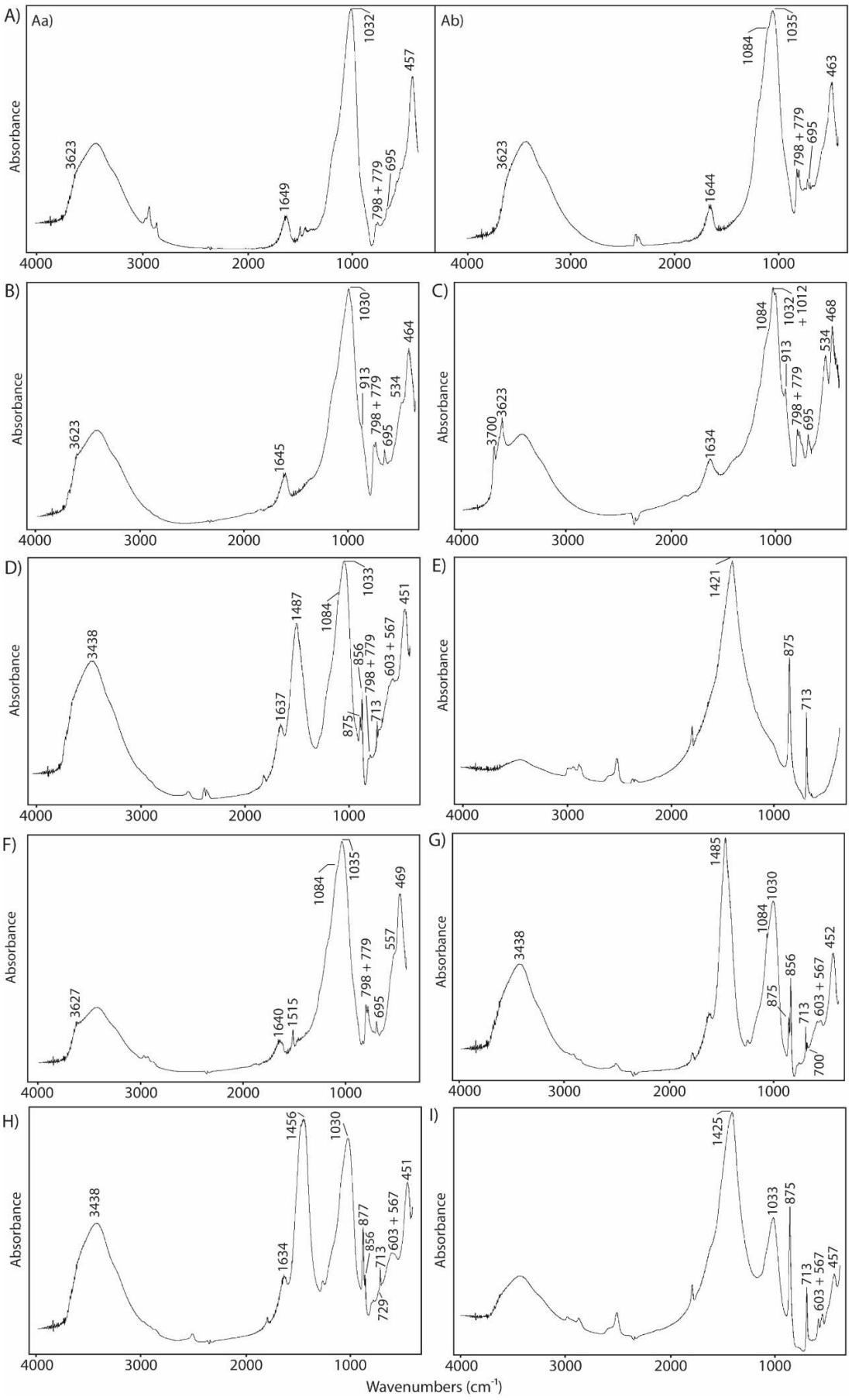

Figure S8. Infrared spectra of lime-rich archaeological contexts according to compositional

groupings (refer to Table S2). Constituents are listed in order of abundance for each spectral group based on relative peak height. A) spectra of altered (heated) clay (absence of the 3700 and 3623cm^{-1} peaks, the 913cm^{-1} peak and the 1012cm^{-1} shoulder, and the shift to higher wavelengths of 1032–1035cm^{-1} of the main Si-O peak), representative of the spectral group A. Left (Aa) Spectra from a micromorphology block sample. Right (Ab) Spectra from a ceramic sherd. Samples within this group may also contain quartz (shown in (Ab) absorbance bands at 1084 and 695cm^{-1} and the strong doublet at 798 and 779cm^{-1}); B) spectra of slightly altered (heated) clay (reduction of absorbance bands at 3700 and 3623cm^{-1} and the 913cm^{-1} shoulder), representative of the spectral group B; C) spectra of unaltered clay (esp. kaolinite) (strong absorbance bands at 3700, 3623 and 1032cm^{-1} and the clear presence of the 913cm^{-1} peak and 1012cm^{-1} shoulder) and quartz (absorbance bands at 1084 and 695cm^{-1} and the doublet at 798 and 779cm^{-1}), representative of the spectral group C; D) spectra of altered (heated) clay (absence of the absorbance bands at 3700 and 3623cm^{-1}, the 913cm^{-1} peak and the 1012cm^{-1} shoulder, and the shift to higher wavenumbers of 1033cm^{-1}of the main Si-O peak), aragonite (main carbonate peak at 1487cm^{-1} with additional bands at 856 and 713cm^{-1}) and calcite (absorbance bands at 875 and 713cm^{-1}), representative of the spectral group D. Note that the location of the v3 *peak at higher wavenumbers (above 1485cm^{-1}) is typical of pyrogenic aragonite, whereas the same peak in geogenic and biogenic aragonite is located at 1475cm^{-1} (Toffolo* et al. *2017: fig. 2). The spectra also contain a small amount of quartz (absorbance bands at 1084cm^{-1} and the doublet at 798 and 779cm^{-1}) and CHAP (weak absorbance bands at 603 and 567cm^{-1}). Samples within this group show a dominant composition of altered (heated) clay and lesser amounts of calcium carbonate (including samples which contain both aragonite and calcite as shown here, or samples containing only calcite); E) calcite (indicative absorbance bands at 1421, 875 and 713cm^{-1}). Spectral image from a shell fragment from a lime mortar floor; F) spectra of altered (heated) clay (absence of the ~3600–3700 cm^{-1} peaks, the 913cm^{-1} peak and the 1012cm^{-1} shoulder, and the shift to higher wavelengths of 1035cm^{-1} of the main Si-O peak) and quartz (absorbance bands at 1084 and 695cm^{-1} and the strong doublet at 798 and 779cm^{-1}), representative of the spectral group F; G) spectra of aragonite (main carbonate peak at 1485cm^{-1} with additional bands at 856 and 713cm^{-1}), calcite (absorbance bands at 875 and 713cm^{-1}) and altered (heated) clay (absence of the absorbance bands at 3700 and 3623cm^{-1}, the 913cm^{-1} peak and the 1012cm^{-1} shoulder), representative of the spectral group G. Note that the location of the* v3 *peak at higher wavenumbers (1485cm^{-1} or above) is typical of pyrogenic aragonite, whereas the*

same peak in geogenic and biogenic aragonite is located at 1475cm^{-1} (Toffolo et al. *2017: fig. 2). The spectra also contain small amounts of quartz (absorbance band at 1084cm^{-1}) and CHAP (weak absorbance bands at 603 and 567cm^{-1}). Samples within this group show a dominant composition of calcium carbonate (including samples which contain both aragonite and calcite as shown here, or samples containing only calcite or only aragonite) and lesser amounts of altered (heated) clay; H) spectra showing a mixture of dolomite (the main carbonate peak at 1456cm^{-1}, the* v2 *peak is at higher wavelengths of 877cm^{-1} and there is an additional peak at 729cm^{-1}), calcite (absorbance bands at 877 and 713cm^{-1}) and aragonite (absorbance bands at 856 and 713cm^{-1}). The spectra also contain altered (heated) clay (absence of the 3700 and 3623cm^{-1} peaks, the 913cm^{-1} peak and the 1012cm^{-1} shoulder) and small amounts of CHAP (absorbance bands at 603 and 567cm^{-1}). Dolomite forms over calcite and aragonite in the presence of magnesium (Mg), thus the detection of dolomite is linked to the presence of Mg in the floor samples (Mg is confirmed in the QEM-EDS elemental maps in Figure S12–S13). There is no known local source of dolomite, for example dolomitic rocks or limestones (Nguyen 1986), thus, we offer two scenarios for the formation of dolomite. 1) dolomite may have formed during diagenesis as a post-depositional replacement of high-Mg calcite or aragonite (Mehmood* et al. *2018); 2) a more speculative scenario is that dolomite has a pyrogenic formation as a primary precipitate during lime carbonation, similar to that of pyrogenic aragonite in lime plasters established by Toffolo and Boaretto (2014). Dolomite may have formed as a result of using shells enriched with Mg-rich sea water to prepare lime. However, shell lime mortar is not well studied in comparison to lime mortars prepared from limestone and the lack of geochemical and microarchaeological studies of shell-made lime mortar precludes a more definitive hypothesis while at the same time necessitates further study including experimental work; I) spectra of calcite (indicative absorbance bands at 1425, 875 and 713cm^{-1}), CHAP (absorbance bands at 603 and 567cm^{-1}) and altered (heated) clay (absence of the 3700 and 3623cm^{-1} peaks, the 913cm^{-1} peak and the 1012cm^{-1} shoulder, and the shift to higher wavelengths of 1033cm^{-1} of the main Si-O peak). Spectral image from a residual lime chunk (F-141) (image by E. Grono).*

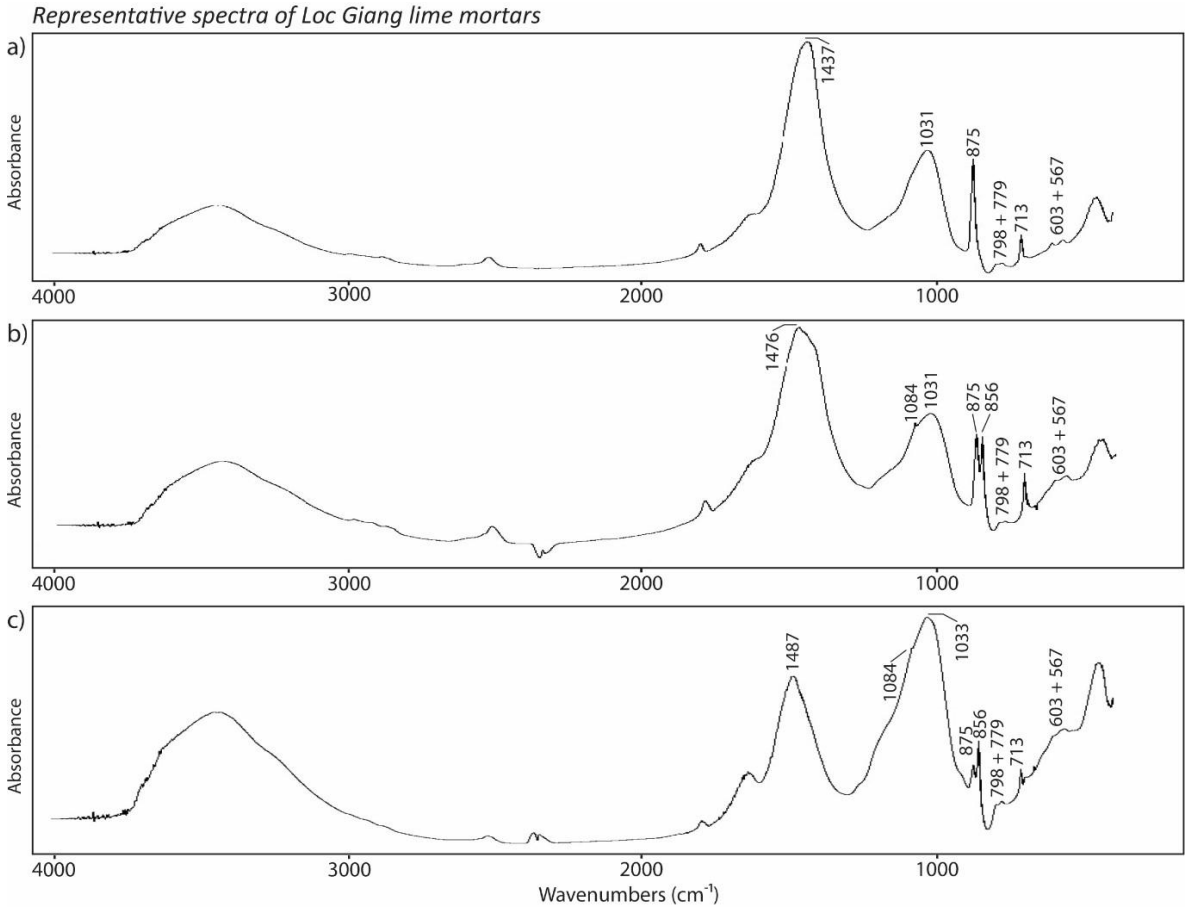

Figure S9. Spectra of lime mortar from Loc Giang floor samples, showing a composition of calcite (main carbonate peak at 1437cm^{-1} with additional bands at 875cm^{-1} and 713cm^{-1}), aragonite (main carbonate peak at 1476cm^{-1} with additional bands at 856cm^{-1} and 713cm^{-1}) and altered (heated) clay (main peak at 1031–1033cm^{-1} and the absence of peaks at ~3600–3700cm^{-1} and 915 cm^{-1} and a shoulder at 1012cm^{-1}). Note that in the spectra shown in (c) the location of the ν3 *peak at higher wavenumbers (above 1485cm^{-1}) is typical of pyrogenic aragonite, whereas the same peak in geogenic and biogenic aragonite is located at 1475cm^{-1} (Toffolo* et al. *2017: fig. 2). The spectra also contain smalls amount of quartz (absorbance bands at 1084cm^{-1} and the doublet at 798 and 778cm^{-1}) and CHAP (weak absorbance bands at 603 and 567cm^{-1}). The Loc Giang spectra closely match reference spectra of archaeological lime mortars (Kimmel Center for Archaeological Science Infrared Standards Library, Weizmann Institute of Science) (image by E. Grono).*

OSM6: biogenic silica concentrations

Table S3. Biogenic silica concentrations of lime-rich archaeological contexts from Loc Giang. A 30 per cent error was calculated in the rightmost column following Katz *et al.* (2010: 1561).

Sample context	Microstratigraphic unit no.	Type of deposit	Phytolith concentrations		Diatom concentrations	
			per 1g sediment	±30% error	per 1g sediment	±30% error
C.100	–	Modern surface sample	676 825	203 047	0	0
F-97	F97.2	Lime mortar floor	446 948	134 084	0	0
F-113	F113.2	Lime mortar floor	632 178	189 653	66 545	19 963
F-117	F117.2	Lime mortar floor	1 390 466	417 140	337 083	101 125
F-141	F141	Residual lime chunk	478 092	143 428	0	0
F-117 (surface coating)	F117.1	Lime plaster coating	1 270 863	381 259	911 706	273 512

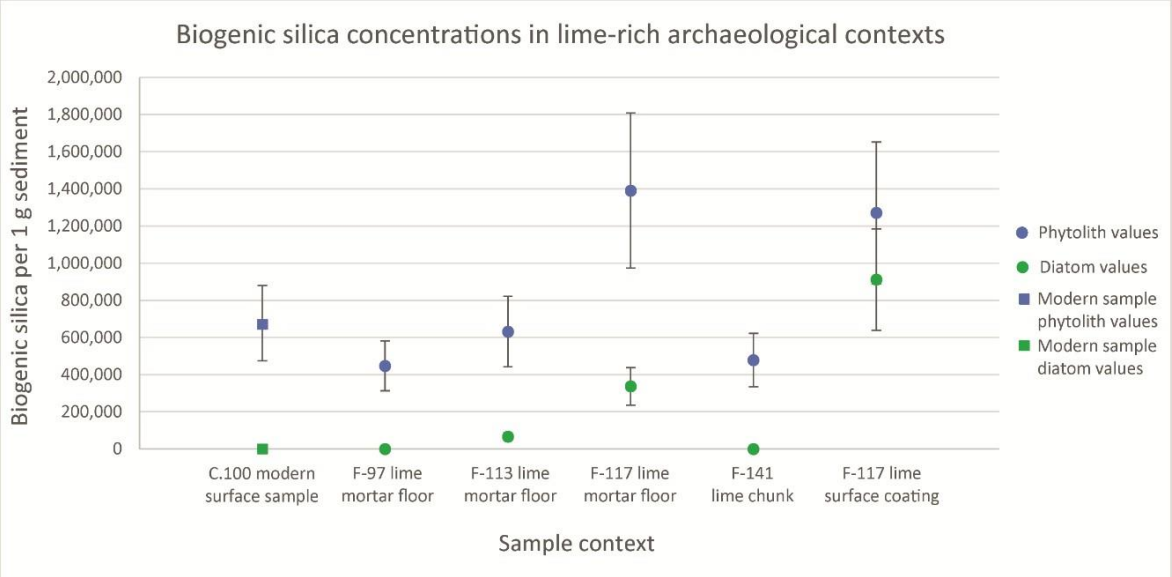

Figure S10. Biogenic silica concentrations of lime-rich archaeological deposits from Loc Giang, depicted according to archaeological feature (F-#) number and deposit type (graph by E. Grono).

OSM7: Automated Quantitative Evaluation of Minerals using Energy Dispersive Spectroscopy (QEM-EDS)

Mineralogical distribution maps

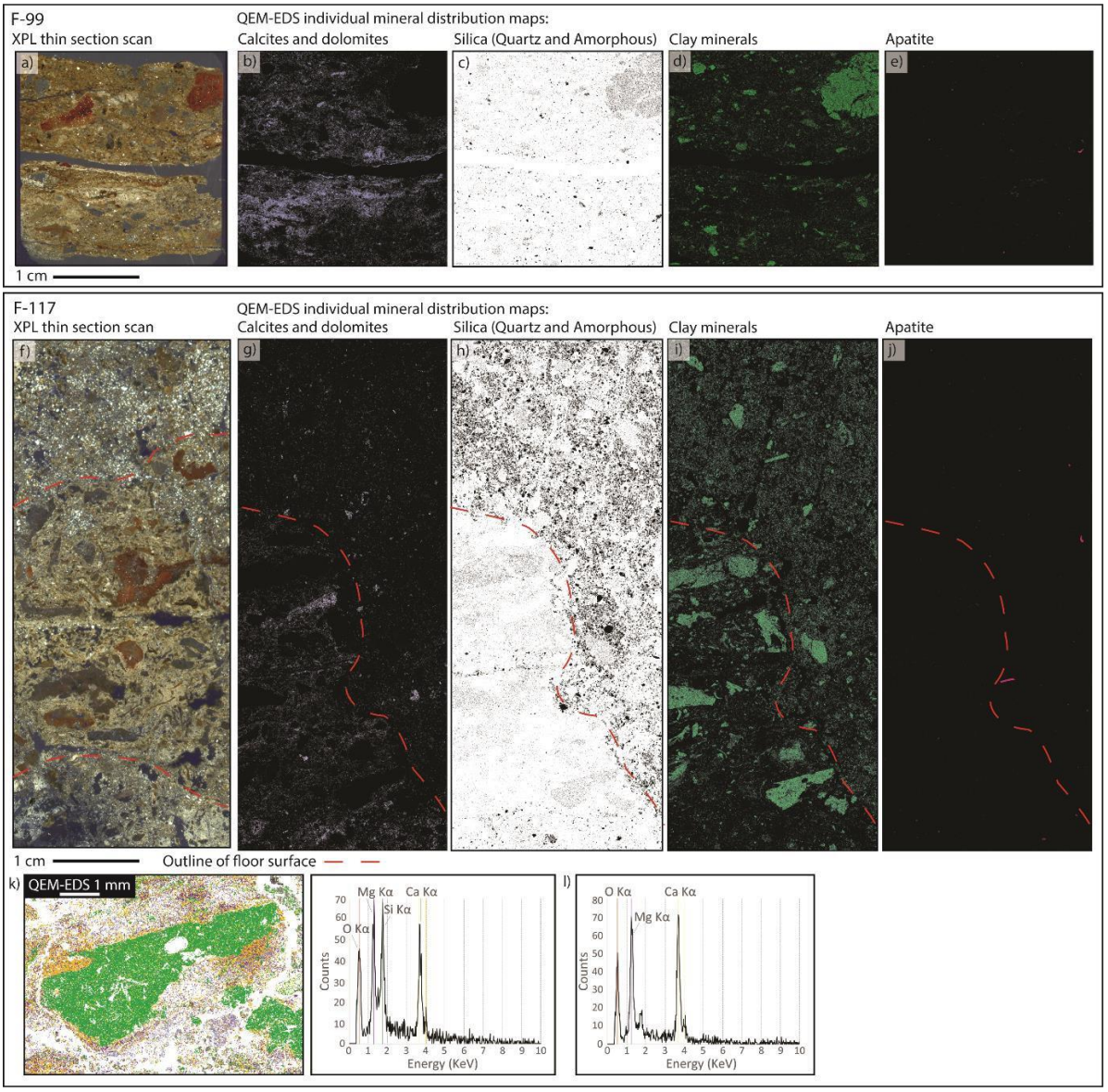

Figure S11. QEM-EDS mineral maps (b–e, g–j) and equivalent XPL thin section scans (a, f) of two floor surfaces: F-99 (a–e) and F-117 (f–j). Note that as the polished QEM-EDS billets were prepared from 'mirror-image' faces of the micromorphology blocks, the QEM-EDS billets and micromorphological thin sections do not exactly match. (a–e) F-99 comprises two superimposed floors and (f–j) F-117 comprises a degraded lime mortar floor (delineated by a dashed red line) and surrounding occupation deposits; (b–e) and (g–j) provide QEM-EDS individual mineral group maps of four major mineral groups: (b) and (g) calcites and dolomites, representing the binder of the floor; (c) and (h) silica, predominantly mineral

quartz grains, infrequent elements in the lime floors and common elements in detrital sediments surrounding the F-117 floor; (d) and (i) clay minerals, including large clay aggregates representing additive materials to the lime floor; and, (e) and (j) apatite, denoting isolated bone fragments as inclusions in the floors and in the sediments surrounding the F-117 floor; k) QEM-EDS mineral scan (left) of a reaction rim of unclassified composition (orange) around a clay aggregate (green). EDS analysis of the rection rim (right) demonstrates a composition of O, Mg, Si and Ca; l) representative EDS spectra of unclassified pixels in the binder (micromass) of the lime floor, showing a composition of O, Mg and Ca (image by E. Grono).

Elemental distribution maps

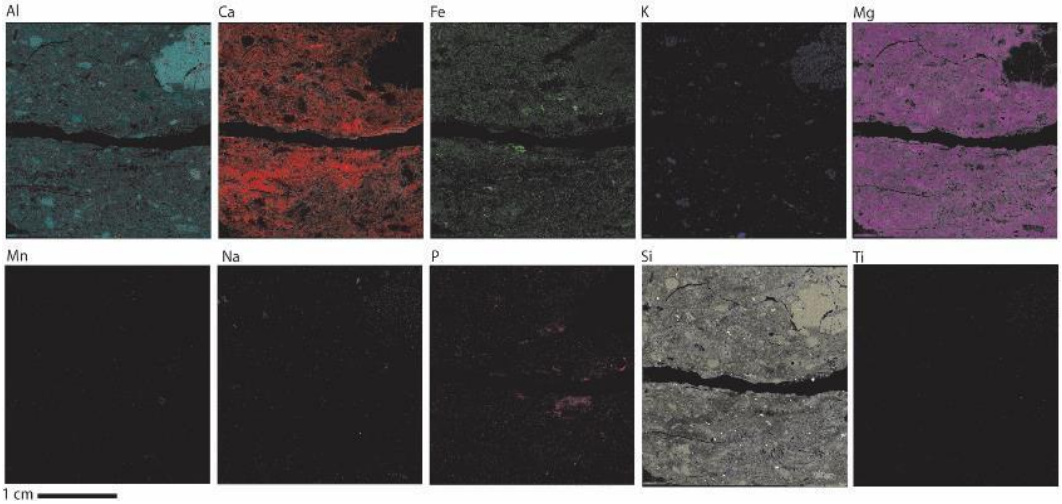

Figure S12. QEM-EDS elemental maps of two superimposed lime mortar floors (F-99) (image by E. Grono).

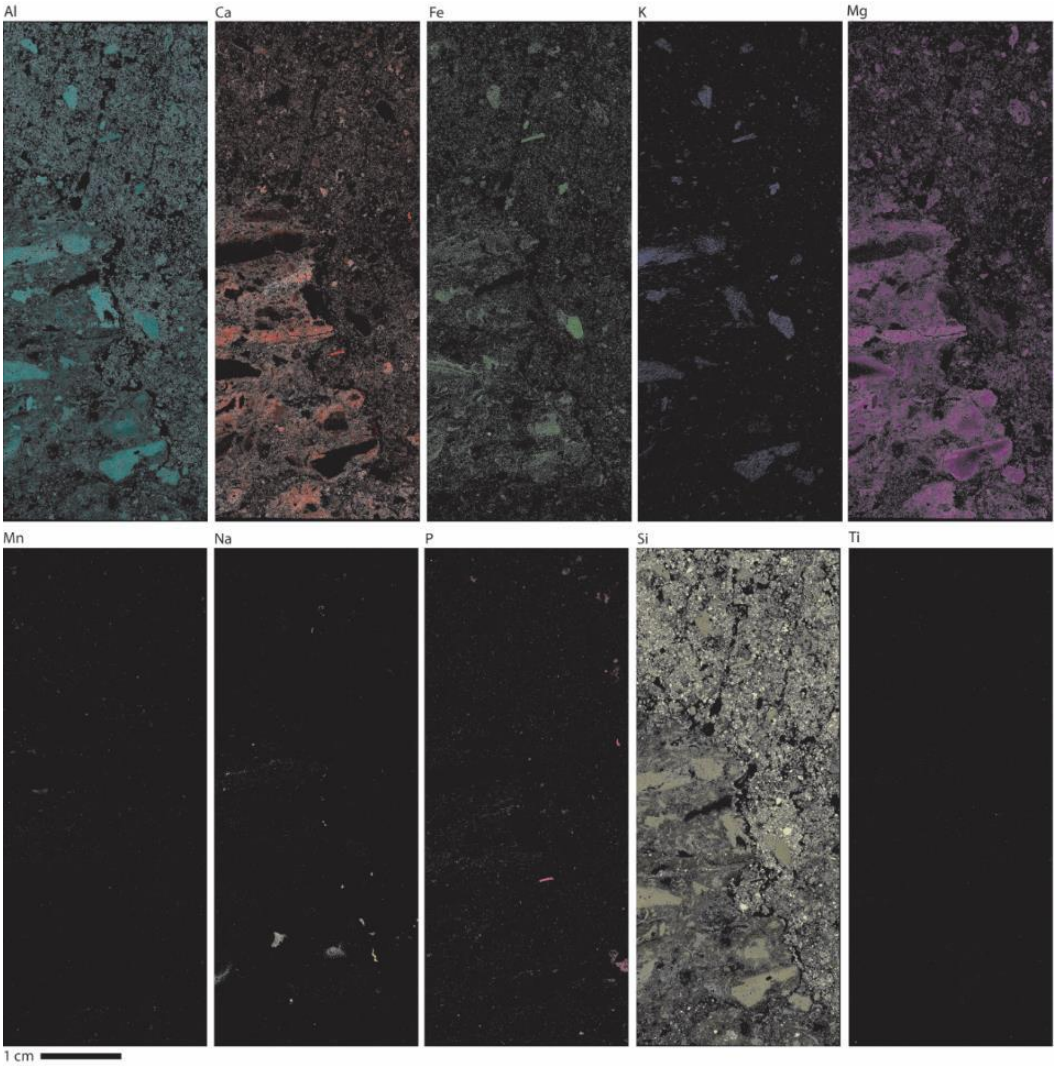

Figure S13. QEM-EDS elemental maps of a degraded lime mortar floor (F-117) and surrounding occupation deposits (#14LGi_6) (image by E. Grono).

References

COURTY, M.-A., P. GOLDBERG & R.I. MACPHAIL. 1989. *Soils and micromorphology in archaeology*. Cambridge: Cambridge University Press. https://doi.org/10.1097/00010694-199012000-00014

KARKANAS, P. 2007. Identification of lime plaster in prehistory using petrographic methods: a review and reconsideration of the data on the basis of experimental and case studies. *Geoarchaeology* 22: 775–96. https://doi.org/10.1002/gea.20186

KATZ, O. *et al*. 2010. Rapid phytolith extraction for analysis of phytolith concentrations and assemblages during an excavation: an application at Tell es- Safi/Gath, Israel. *Journal of Archaeological Science* 37: 1557–63. https://doi.org/10.1016/j.jas.2010.01.016

MACPHAIL, R.I. & P. GOLDBERG. 2017. *Applied soils and micromorphology in archaeology*. Cambridge: Cambridge University Press. https://doi.org/10.1017/9780511895562

MOORE, D.M. & J. REYNOLDS. 1989. *X-Ray Diffraction and the identification and analysis of clay minerals*. Oxford: Oxford University Press.

MEHMOOD, M., M. YASEEN, E.U. KHAN & J.M. KHAN. 2018. Dolomite and dolomitization model: a short review. *International Journal of Hydrology* 2: 549–53. https://doi.org/10.15406/ijh.2018.02.00124

NICOSIA, C. & G. STOOPS. 2017. *Archaeological soil and sediment micromorphology*. Hoboken (NJ): Wiley. https://doi.org/10.1002/9781118941065

NGUYEN, X.B. 1986. *Geological map of the continental part of Vietnam* [volume of cartographic material, 1:1 500.000 scale]. Hanoi: The Department of Geological Mapping, General Department of Geology, Socialist Republic of Vietnam.

STOOPS, G. 2003. *Guidelines for analysis and description of soil and regolith thin sections*. Madison (WI): Soil Science Society of America.

STOOPS, G., M. CANTI & S. KAPUR. 2017. Calcareous mortars, plasters and floors, in C. Nicosia & G. Stoops (ed.) *Archaeological soil and sediment micromorphology*: 189–99. Hoboken (NJ): Wiley. https://doi.org/10.1002/9781118941065.ch23

TOFFOLO, M.B. & E. BOARETTO. 2014. Nucleation of aragonite upon carbonation of calcium oxide and calcium hydroxide at ambient temperatures and pressures: a new indicator of fire-related human activities. *Journal of Archaeological Science* 49: 237–48. https://doi.org/10.1016/j.jas.2014.05.020

TOFFOLO, M.B. *et al*. 2017.Accurate radiocarbon dating of archaeological ash using pyrogenic aragonite. *Radiocarbon* 59: 231–49. https://doi.org/10.1017/RDC.2017.7

WEINER, S. 2010. *Microarchaeology: beyond the visible archaeological record*. Cambridge:

Cambridge University Press. https://doi.org/10.1017/CBO9780511811210